Monthly Notices
of the
ROYAL ASTRONOMICAL SOCIETY

MNRAS **461,** 3886–3895 (2016)
Advance Access publication 2016 June 26

doi:10.1093/mnras/stw1484

Mean Hα+[N II]+[S II] EW inferred for star-forming galaxies at $z \sim 5.1$–5.4 using high-quality *Spitzer*/IRAC photometry

N. Rasappu,[1⋆] R. Smit,[2⋆] I. Labbé,[1] R. J. Bouwens,[1⋆] D. P. Stark,[3] R. S. Ellis[4] and P. A. Oesch[5]

[1]*Leiden Observatory, Leiden University, NL-2300 RA Leiden, the Netherlands*
[2]*Department of Physics, Durham University, South Road, Durham DH1 3LE, UK*
[3]*Department of Astronomy/Steward Observatory, 933 North Cherry Avenue, Tucson, AZ 85721, USA*
[4]*Cahill Center for Astronomy and Astrophysics, California Institute of Technology, MC 249-17, Pasadena, CA 91125, USA*
[5]*Department of Astronomy, Yale University, New Haven, CT 06520, USA*

Accepted 2016 June 17. Received 2016 June 13; in original form 2015 August 18

ABSTRACT

Recent *Spitzer*/InfraRed Array Camera (IRAC) photometric observations have revealed that rest-frame optical emission lines contribute significantly to the broad-band fluxes of high-redshift galaxies. Specifically, in the narrow redshift range $z \sim 5.1$–5.4 the [3.6]–[4.5] colour is expected to be very red, due to contamination of the 4.5 μm band by the dominant Hα line, while the 3.6 μm filter is free of nebular emission lines. We take advantage of new reductions of deep *Spitzer*/IRAC imaging over the Great Observatories Origins Deep Survey-North+South fields (Labbé et al. 2015) to obtain a clean measurement of the mean Hα equivalent width (EW) from the [3.6]–[4.5] colour in the redshift range $z = 5.1$–5.4. The selected sources either have measured spectroscopic redshifts (13 sources) or lie very confidently in the redshift range $z = 5.1$–5.4 based on the photometric redshift likelihood intervals (11 sources). Our $z_{\rm phot} = 5.1$–5.4 sample and $z_{\rm spec} = 5.10$–5.40 spectroscopic sample have a mean [3.6]–[4.5] colour of 0.31 ± 0.05 and 0.35 ± 0.07 mag, implying a rest-frame EW (Hα+[N II]+[S II]) of 665 ± 53 and 707 ± 74 Å, respectively, for sources in these samples. These values are consistent albeit slightly higher than derived by Stark et al. at $z \sim 4$, suggesting an evolution to higher values of the Hα+[N II]+[S II] EW at $z > 2$. Using the 3.6 μm band, which is free of emission line contamination, we perform robust spectral energy distribution fitting and find a median specific star formation rate of sSFR $= 17^{+2}_{-5}$ Gyr^{-1}, $7^{+1}_{-2}\times$ higher than at $z \sim 2$. We find no strong correlation ($<2\sigma$) between the Hα+[N II]+[S II] EW and the stellar mass of sources. Before the advent of *JWST*, improvements in these results will come through an expansion of current spectroscopic samples and deeper *Spitzer*/IRAC measurements.

Key words: galaxies: evolution – galaxies: formation – galaxies: high-redshift.

1 INTRODUCTION

In recent years, large multiwavelength photometric surveys conducted with the *Hubble* and *Spitzer Space Telescopes* have enabled us to study the properties of galaxies over cosmic time. Synthetic stellar population modelling of broad-band spectral energy distributions (SEDs) has led to the determination of various physical properties (e.g. stellar mass, star formation rate – SFR, age, dust extinction) of these galaxies (Eyles et al. 2005; Yan et al. 2006; Bouwens et al. 2009, 2012; Stark et al. 2009; González et al. 2010; Finkelstein et al. 2012; Oesch et al. 2013; Castellano et al. 2014; de Barros, Schaerer & Stark 2014; Salmon et al. 2015). Of all derived quantities, stellar masses are particularly robust in stellar population fits. Small changes in the age of the stellar populations, metallicity or other parameters have no significant effect on the estimated masses (e.g. Finlator, Davé & Oppenheimer 2007; Yabe et al. 2009).

Considerable progress has been made in refining current characterization of galaxies from the observations. Even so, the measurements of the specific star formation rate (sSFR, the SFR divided by the stellar mass) have presented a puzzle to the theoretical understanding of the build-up of mass in galaxies (e.g. Bouché et al.

⋆E-mail: nicholasrasappu@gmail.com (NR); renske.smit@durham.ac.uk (RS); bouwens@strw.leidenuniv.nl (RJB)

2010; Weinmann, Neistein & Dekel 2011). Several past studies had indicated that the sSFR of sources with fixed stellar mass shows no evidence for significant evolution between $z \simeq 2$ and $\simeq 7$ (Stark et al. 2009; González et al. 2010). This result was in apparent disagreement with semi-analytic models predicting a strong increase in the specific inflow rate (i.e. inflow rate divided by halo mass) of baryons with redshift (Neistein & Dekel 2008).

Subsequent work has strongly suggested that the sSFR of galaxies is somewhat higher at $z > 2$ than it is at $z \sim 2$ (e.g. Schaerer & de Barros 2010; Stark et al. 2013; González et al. 2014; Salmon et al. 2015). The change in the inferred sSFR evolution with cosmic time was the result of improved observational constraints and a more sophisticated treatment of those constraints. One example of this is in a consideration of dust extinction in computing the sSFRs at $z > 2$. While it was not possible to account for the impact of dust extinction in initial work (e.g. González et al. 2010) due to large uncertainties on the *UV* colours of $z > 2$ galaxies, later work (Bouwens et al. (2012) was able to make use of new measurements of the *UV* continuum slopes to account for the impact of dust extinction, assuming that the direct relation between far-infrared excess and the *UV* continuum slope of local star-bursting galaxies (e.g. Meurer, Heckman & Calzetti 1999) holds for high-redshift UV selected galaxies, thus finding $\sim$2 $\times$ larger sSFRs at $z \geq 4$. This suggested a 2 $\times$ evolution relative to the $z \sim 2$ value (Reddy et al. 2012b), but still leaving the sSFR at $z > 4$ approximately constant.

Even more important has been the increasing awareness of the impact of rest-frame optical nebular emission lines (e.g. Hα, [O III], [O II]) on the broad-band fluxes (e.g. Schaerer & de Barros 2009, 2010; Schenker et al. 2013). At high redshifts, these emission lines are shifted into the infrared, contaminating the InfraRed Array Camera (IRAC) measurements of the stellar continuum. Inferred stellar masses from fitting of stellar population models will then be overestimated, resulting in an underestimate of the sSFR.

Since these strong rest-frame optical lines are inaccessible to spectroscopy beyond $z \sim 2$–3, the strength of the nebular emission lines has been estimated from the contamination of the *Spitzer*/IRAC 3.6 and 4.5 μm bands for galaxies at $z > 3$. Shim et al. (2011) show that galaxies in the range $3.8 < z < 5.0$ are considerably brighter at 3.6 μm than expected from the stellar continuum alone and argue that this excess is due to strong Hα line emission. Stark et al. (2013) derive an Hα equivalent width (EW) distribution by comparing the [3.6]–[4.5] colour of spectroscopically confirmed galaxies in the redshift range $3.8 < z < 5.0$, where the Hα line lies in the 3.6 μm band, with an uncontaminated control sample at $3.1 < z < 3.6$. The results indicate a possible trend towards higher Hα EWs at higher redshifts, which is extremely important for estimating the sSFR at $z > 5$ (see also Labbé et al. 2013; de Barros et al. 2014; Smit et al. 2014, 2015a). Independent evidence for high-EW nebular lines having a large impact on the broad-band fluxes of $z > 3$ galaxies was obtained from early near-infrared, multi-object spectroscopic campaigns (e.g. Schenker et al. 2013; Holden et al. 2016).

The highest redshift window providing us a largely clean measurement of the Hα EW is the redshift range $z \sim 5.10$–5.40. Here, the flux excess due to the redshifted nebular emission lines gives rise to significantly redder [3.6]–[4.5] colours over this range, making it possible to quantify the EW of Hα at $z > 5.1$ in a similar way to that possible in the redshift range $z = 3.8$–5.0. By examining the [3.6]–[4.5] colour of galaxies from the Bouwens et al. (2015) catalogue (see Section 3.1) over the Great Observatories Origins Deep Survey (GOODS)-North and South fields (Giavalisco et al. 2004) in this highest redshift window $z \sim 5.1$–5.4 where Hα can be cleanly measured,[1] we can derive approximate constraints on the Hα flux and EW at the highest redshift currently accessible at reasonable S/N with current facilities. This allows us to obtain better constraints on the evolution of the mean Hα EW and sSFR as a function of redshift.

This paper is structured as follows. In Section 2, we describe the observational data sets and our photometric selection of sources in the narrow redshift range. In Section 3, we examine our selected sample of galaxies. We describe the assumptions made in deriving the EWs and sSFRs. Finally, in Section 4, we discuss our results and give a summary. We refer to the *Hubble Space Telescope* (*HST*) *F435W*, *F606W*, *F775W*, *F814W*, *F850LP*, *F105W*, *F125W*, and *F160W* bands as B_{435}, V_{606}, i_{775}, I_{814}, z_{850}, Y_{105}, J_{125} and H_{160}, respectively. For consistency with previous work, we adopt the concordance model with $\Omega_{\rm m} = 0.3$, $\Omega_{\Lambda} = 0.7$ and $H_0 = 70\,{\rm km\,s^{-1}\,Mpc^{-1}}$. Throughout, we assume a Salpeter (1955) initial mass function (IMF) between 0.1 and 100 $M_{\odot}$. All magnitudes are quoted in the AB photometric system (Oke & Gunn 1983).

2 OBSERVATIONS

2.1 Data

In order to select sources in the redshift range $z \sim 5.1$–5.4, we make use of the deep optical/Advanced Camera for Surveys (ACS) and near-infrared/WFC3/IR observations over the GOODS-North and GOODS-South fields from three significant *HST* programmes: GOODS, ERS (Early Release Science; Windhorst et al. 2011), and CANDELS (Cosmic Assembly Near-infrared Deep Extragalactic Legacy Survey; Grogin et al. 2011; Koekemoer et al. 2011). The moderately deep regions over the CANDELS GOODS-North and South reach a 5σ depth of $\sim$ 27.5 mag in the Y_{105}, J_{125} and H_{160} filters with the *HST* and cover $\sim$ 100 arcmin^2. The deep regions over the CANDELS GOODS-North and South reach a 5σ depth of $\sim$ 28.5 in the Y_{105}, J_{125} and $H_1$60 bands, covering $\sim$ 125 arcmin^2 (Grogin et al. 2011). *HST* observations with the ACS are available in the B_{435}, V_{606}, i_{775}, I_{814} and z_{850} bands, up to $\sim$ 29 mag at 5σ in I_{814} (Bouwens et al. 2015). Over the northern $\sim$40 arcmin^2 section of GOODS South (Windhorst et al. 2011), deep near-IR observations are available ($\sim$28 mag at 5σ) in the Y_{098}, J_{125}, and H_{160} bands and also in the B_{435}, V_{606}, i_{775} and z_{850} bands with ACS. The observations are point spread function (PSF) matched to the H_{160} band before measuring the colours in scalable Kron (1980) apertures.

Essential to the analysis, we take advantage of the 3.6 and 4.5 μm IRAC observations from the *Spitzer Space Telescope*. *Spitzer*/IRAC data is from the original GOODS programme, the *Spitzer* Extented Deep Survey (SEDS; Ashby et al. 2013), the *Spitzer* Very Deep Survey (S-CANDELS; Ashby et al. 2015) Exploration Science Project, the IUDF10 programme (Labbé et al. 2015), and other programmes (such as PID10076, PI: Oesch). The *Spitzer*/IRAC reductions we utilize were generated by Labbé et al. (2015) and feature a 1.8 arcsec-diameter full width at half-maximum for the PSF.

Deblending neighbouring galaxies in the IRAC observations and PSF corrections are performed using the MOPHONGO software (Labbé et al. 2010a,b, 2013, 2015). *HST* *F160W* images are used as a high resolution prior to construct a model for the contaminating

[1] At $z \gtrsim 5.5$, constraints on the H α EWs are also possible from Spitzer/IRAC observations, but would need to rely on the stacking the fluxes of $z \gtrsim 5.5$ galaxies in the much less sensitive 5.8 μm band.

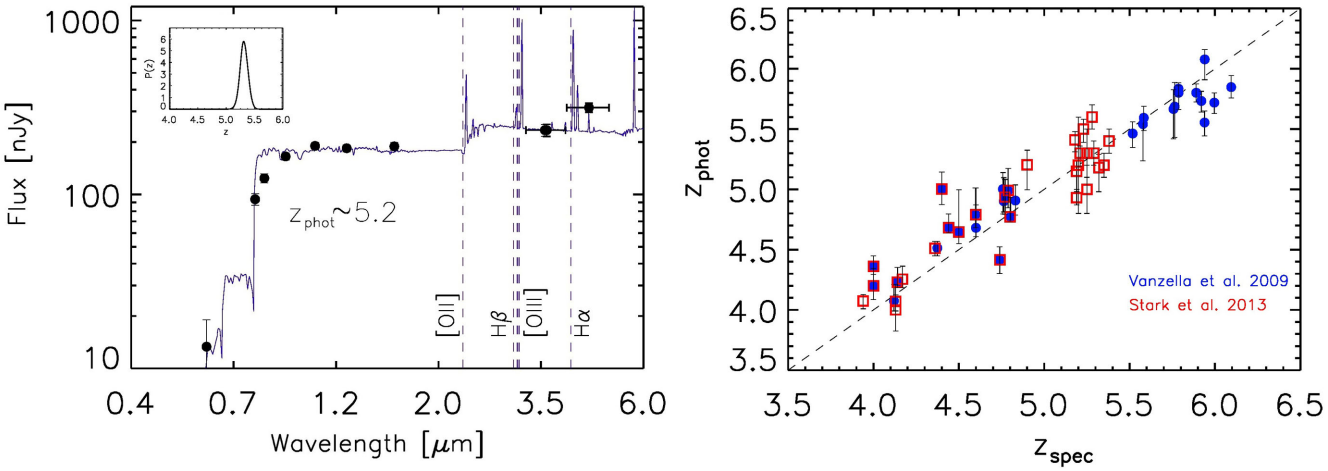

Figure 1. Left-hand panel: model SED (blue) and the *HST* flux measurements (black dots) for one of the sources in our selection fitted with the photometric redshift code EAZY (Brammer, van Dokkum & Coppi 2008). Displayed in the upper-left corner: the cumulative probability distribution P(z) to find the galaxies at a certain redshift. We only use candidates with $P(5.1 < z < 5.4) > 0.85$. The *Spitzer*/IRAC bands are not included in the fitting to prevent bias in the [3.6]–[4.5] colours. Right-hand panel: photometric redshift as determined by EAZY against spectroscopic redshift for the sources in Vanzella et al. (2009, blue points) and Stark et al. (2013, red squares). At $z \lesssim 5$, EAZY seems to overestimate the redshift by $\Delta z/(1+z) \sim 0.02$, while the redshift is underestimated by $\Delta z/(1+z) \gtrsim 0.03$ for $z \gtrsim 6.0$. Though we need a far larger sample to confirm the presence of such an offset, the redshift window that we are considering is seemingly the least affected.

sources, while leaving the normalization of the sources as a free parameter. The fluxes of all sources in a radius of 13 arcsec are then simultaneously fit to best match the IRAC image. Beyond a radius of 13 arcsec the faint wings of the PSF used for convolving the high-resolution image contributes negligible flux, see Labbé et al. (2015), and therefore objects beyond this radius will not affect our final photometry. Photometry is then performed within a 2.0 arcsec diameter aperture. The deep IRAC imaging from S-CANDELS reaches ∼26.8 mag at 5σ in the 3.6 μm band.

For $z = 5.1$–5.4 sources not included in the photometric catalogues of Bouwens et al. (2015 : due to their being located in areas of the GOODS fields without B_{435} or Y_{098}/Y_{105}-band observations), we made use of the *HST* photometry from the 3D-*HST* GOODS-North or GOODS-South catalogues (Skelton et al. 2014). This is relevant for 5 $z = 5.1$–5.4 galaxies in our final sample. We refer to Skelton et al. (2014) for a detailed description.

2.2 Photometric redshift selection

The Lyman-break selection criteria applied for sources at $z \sim 5$ is as follows:

$$(V_{606} - i_{775} > 1.2) \wedge (z_{850} - H_{160} < 1.3) \wedge$$
$$(V_{606} - i_{775} > 0.8\,(z_{850} - H_{160}) + 1.2),$$

where $\wedge$ denotes the AND symbol. For non-detections, the 1σ upper limit is taken as the flux in the dropout band. The aforementioned criteria enable to select sources in the range $z \sim 4.5$–5.5. Therefore, a high-redshift boundary is set by excluding sources which satisfy the selection criteria for $z \sim 6$ selection (e.g. Bouwens et al. 2015a). Contamination from sources at lower redshifts is reduced by requiring that the $z \sim 5$ sources have a non-detection ($< 2\sigma$) in the B_{435} band. Furthermore, we exclude point sources by requiring the SExtractor stellarity index to be less than 0.9 (where 0 and 1 correspond to extended and point sources, respectively). Utilizing these selection criteria results in an initial *V*-drop sample of 1567 sources (Bouwens et al. 2015).

In order to be able to measure the Hα EW for $z \gtrsim 5$ galaxies, it is easiest to only make use of galaxies in the narrow redshift window $z = 5.10$–5.40. We therefore use photometric redshifts to identify a subsample of galaxies in this window. The photometric redshifts for our sample are determined using the EAZY photometric redshift code (Brammer et al. 2008), which compares photometric data with synthetic photometry of galaxies for various template spectra and redshift ranges. The best-fitting redshift is then derived from a statistical analysis of the differences between both data sets. The aforementioned eight *HST* bands (B_{435}, V_{606}, i_{775}, I_{814}, z_{850}, Y_{105}, J_{125}, H_{160}) are used to derive the best-fitting photmetric redshifts. The IRAC photometry is excluded from this fitting to avoid introducing any bias in the measured [3.6]–[4.5] colour. This reduces the sample size to 393 sources.

Fig. 1 shows an example output of EAZY for a source at $z \sim 5.2$ and a comparison of our estimated EAZY photometric redshifts for a sample of $z = 4$–6 spectroscopically confirmed sources from Stark et al. (2010: see Stark et al., in preparation) and Vanzella et al. (2009) over the GOODS North and South fields. The scatter around the one-to-one relation is $\Delta z/(1+z) = 0.036$, which provides confidence that we can select sources in the narrow redshift range $z = 5.1$–5.4.

We select very bright sources with the requirements that S/N(H_{160}) $> 7 \wedge$ S(H_{160})/N(3.6 μm) $> 3 \wedge$ S(H_{160})/N(4.5 μm) > 3, where S/N is the signal-to-noise ratio. Our selection of sources based on their measured flux in the H_{160} band and measured noise in the *Spitzer*/IRAC bands allows us to include sources in our analysis which we would expect to show up prominently in the *Spitzer*/IRAC bands. Basing the selection on the measured flux in the *Spitzer*/IRAC bands would bias our measurement of the colours. We also discard 41 sources for which the contamination by nearby objects is higher than 200 nJy or sources with a poor IRAC deblending (χ^2 parameter less than 0.2), reducing the sample to 101 bright sources.

Finally, we require that the EAZY redshift probability distribution prefers a redshift in the range $z = 5.1$–5.4 at >85 per cent, providing a sample with 11 sources in the redshift range $z \sim 5.1$–5.4 presented

Table 1. Our selections of sources with a high probability of lying in the redshift range $5.1 < z < 5.4$ from the photometry.[a]

ID	RA	Dec.	$z_{\rm phot}^{b}$	[3.6] (mag)	[3.6]–[4.5] (mag)	Hα+[N II]+[S II] EW (Å)[c]	sSFR ($\rm Gyr^{-1}$)	$\log_{10}M$ ($\rm M_{\odot}$)	$M_{\rm UV}^{d}$
GNDV-7133823953	12:37:13.38	62:12:39.5	5.2 ± 0.1	26.0 ± 0.2	0.5 ± 0.3	672 ± 505	30^{+10}_{-9}	$8.84^{+0.12}_{-0.11}$	-21.3 ± 0.1
GNDV-7128013231	12:37:12.80	62:11:32.3	5.3 ± 0.2	25.3 ± 0.1	0.1 ± 0.2	190 ± 254	17^{+12}_{-6}	$9.24^{+0.30}_{-0.13}$	-20.8 ± 0.1
GNDV-7033233179[e]	12:37:03.32	62:13:31.8	5.3 ± 0.1	25.9 ± 0.1	0.4 ± 0.2	719 ± 368	24^{+8}_{-11}	$8.93^{+0.10}_{-0.17}$	-20.8 ± 0.1
GNDV-6302234526	12:36:30.22	62:13:45.3	5.2 ± 0.1	25.3 ± 0.1	0.3 ± 0.1	385 ± 170	11^{+6}_{-8}	$9.38^{+0.19}_{-0.28}$	-20.6 ± 0.1
GNDV-6285841077	12:36:28.58	62:14:10.8	5.3 ± 0.1	26.2 ± 0.1	0.2 ± 0.2	557 ± 449	21^{+17}_{-11}	$8.76^{+0.32}_{-0.20}$	-20.7 ± 0.1
GNWV-6514085687	12:36:51.40	62:08:56.9	5.3 ± 0.1	24.7 ± 0.1	0.0 ± 0.1	25 ± 167	1^{+1}_{-1}	$10.12^{+0.06}_{-0.00}$	-20.6 ± 0.1
GNWV-6121502518	12:36:12.15	62:10:25.2	5.3 ± 0.1	25.8 ± 0.2	0.4 ± 0.3	917 ± 573	6^{+5}_{-10}	$9.29^{+0.25}_{-0.62}$	-20.8 ± 0.1
GNWV-6095211615	12:36:09.52	62:11:16.2	5.2 ± 0.1	25.0 ± 0.1	0.4 ± 0.1	913 ± 274	19^{+12}_{-10}	$9.24^{+0.27}_{-0.20}$	-21.6 ± 0.1
GNDV-3756634257	12:37:05.66	62:13:42.6	5.3 ± 0.1	25.3 ± 0.1	0.1 ± 0.1	274 ± 180	26^{+11}_{-19}	$9.55^{+0.15}_{-0.29}$	-21.2 ± 0.1
GNDV-6325033158	12:36:32.50	62:13:31.6	5.3 ± 0.1	25.8 ± 0.1	0.4 ± 0.1	882 ± 262	9^{+5}_{-3}	$8.79^{+0.24}_{-0.07}$	-20.9 ± 0.1
GSDV-2332672480	03:32:33.26	−27:47:24.8	5.3 ± 0.1	24.8 ± 0.1	0.6 ± 0.1	1480 ± 110	1^{+1}_{-1}	$10.06^{+0.06}_{-0.01}$	-20.6 ± 0.1

Notes. [a]To identify those sources with the highest probability of lying in the redshift range $z = 5.10$–5.40, sources are required to have $P(5.1 < z < 5.4) > 0.85$.
[b]Uncertainties indicate the 68 per cent confidence interval.
[c]The estimated EW for individual sources is derived by comparing the 4.5 μm flux with that derived from FAST (excluding the 4.5 μm flux from the fits).
[d]The z_{850} band magnitude is used to derive the intrinsic UV luminosity.
[e]Spectroscopically confirmed to be at $z = 5.21$ (Stark et al., in preparation).

in Table 1. We show an example of a photometric redshift selected source in Fig. 1

2.3 Spectroscopic redshift selection

In addition to making use of sources very likely to lie in the redshift range $z = 5.1$–5.4 using our photometry for the sources and the redshift likelihood distributions we derive, we can also make use of sources known to lie in the redshift range $z = 5.1$–5.4 from available spectroscopy (Stark et al., in preparation). Using spectroscopic redshifts, we can be even more certain that the sources we are using lie in the narrow redshift range $z = 5.10$–5.40 required for our desired measurement of the Hα flux.

One potential drawback to the inclusion of such sources in the present study is that we might be working with a biased sample, given that essentially all of the spectroscopic redshift measurements we utilize come from Lyα, and it is not clear a priori that the study of such a sample might bias the mean Hα EW we measure to higher values. Fortunately, as we show in a separate study (Smit et al. 2015b), the mean Hα+[N II]+[S II] EW measured for both photometric-redshift and spectroscopic samples are essentially identical.

Cross-correlating the source catalogues of Bouwens et al. (2015) and Skelton et al. (2014) with the spectroscopic catalogue of Stark et al. (in preparation) and Vanzella et al. (2009), we identified 13 $z = 5.10$–5.40 galaxies that we can use for our study, with only one source overlapping with our photometric selection (see Table 2).

The small overlap between our spectroscopic-redshift-selected sample and our photometric-redshift-selected sample is not a concern and is due to the challenge in isolating sources in the narrow redshift interval $z = 5.1$–5.4 based on their photometry. While we observe the excellent overall agreement between the photometric redshifts we derive for sources and their spectroscopic redshifts (Fig. 1), only one source in our spectroscopic-redshift selected sample (Table 2) have estimated redshifts which lie at the centre of the redshift interval $z = 5.1$–5.4 and which are sufficiently narrow such that 85 per cent of the redshift likelihood lies between $z = 5.1$ and 5.4. Based on the information in Table 2, it should be obvious that at least 10 sources from our spectroscopic sample would miss our photometric selection.

As in our photometric redshift selection (Section 2.2), we exclude sources where flux from neighbouring sources significantly contaminate the photometric apertures for our $z = 5.10$–5.40 sample (three sources). 10 of the sources in the desired redshift range were from Stark et al. (in preparation) redshift compilation, while three came from the Vanzella et al. (2009) compilation.

We will make use of sources from both our high-quality photometric redshift sample and spectroscopic sample for the analyses that follows.

3 RESULTS

Using the selection discussed in Sections 2.2 and 2.3, we have isolated a sample of 24 galaxies that have redshifts in the narrow redshift range $z \sim 5.1$–5.4 at high confidence. In this section, we will discuss the IRAC [3.6]–[4.5] colours of these galaxies and compare them with the IRAC colours of a spectroscopically confirmed sample of $z \sim 4.5$ galaxies.

3.1 Mean [3.6]–[4.5] colour for $z = 5.1$–5.4 Galaxies

Our selection of galaxies in the redshift range $z \sim 5.1$–5.4 allows us to solve for the rest-frame EW of the nebular emission lines using the [3.6]–[4.5] colour. Assuming $F_\nu \approx$ constant (i.e. $F_\lambda \propto \lambda^{-2}$), we approximate the observed flux $F_{\nu,\,\rm obs}$ in the IRAC filters, for a given EW, by

$$F_{\nu,\rm obs} = F_{\nu,\rm continuum} \times x_{\rm EW} = \left(1 + \sum_{\rm lines,\,i} \frac{\rm EW_{0,\,i} \cdot (1+z) \cdot R(\lambda_{\rm obs,\,i})}{\lambda_{\rm obs,\,i} \int R(\lambda)/\lambda \, {\rm d}\lambda}\right), \quad (1)$$

where $F_{\nu,\,\rm continuum}$ is the stellar continuum flux and $\lambda_{\rm obs,\,i}$ is the observed wavelength of the nebular emission lines (Smit et al. 2014). $R(\lambda)$ denotes the response curve of the filter. We use all nebular emission lines tabulated in Anders & Fritze-v. Alvensleben (2003) and the hydrogen Balmer lines for the modelling of the [3.6]–[4.5] colour. We fix the line intensities relative to Hβ according to the

Table 2. Sample of spectroscopically confirmed sources in the redshift range $5.1 < z < 5.4$.[a]

ID	RA	Dec.	$z^a_{\rm spec}$	$z^b_{\rm phot}$	[3.6] (mag)	[3.6]–[4.5] (mag)	Hα+[N II]+[S II] EW (Å)[c]	sSFR ($\rm Gyr^{-1}$)	$\log_{10}M$ ($\rm M_\odot$)	$M_{\rm UV}$
GNDV-6554953313	12:36:55.49	62:15:33.1	5.19	4.9 ± 0.1	25.5 ± 0.2	0.6 ± 0.2	1579 ± 359	10^{+6}_{-7}	$9.09^{+0.24}_{-0.28}$	-21.3 ± 0.1
GNDV-7033233179	12:37:03.32	62:13:31.8	5.21	5.3 ± 0.1	25.9 ± 0.1	0.4 ± 0.2	719 ± 368	24^{+8}_{-11}	$8.93^{+0.10}_{-0.17}$	-20.8 ± 0.1
GNDV-7027322916	12:37:02.73	62:12:29.2	5.23	5.5 ± 0.1	25.4 ± 0.1	0.5 ± 0.1	1000 ± 257	37^{+12}_{-16}	$9.21^{+0.06}_{-0.13}$	-20.6 ± 0.1
GNDV-6375223629	12:36:37.52	62:12:36.3	5.18	5.4 ± 0.1	25.7 ± 0.2	0.0 ± 0.3	<419[d]	21^{+19}_{-35}	$8.62^{+0.35}_{-0.71}$	-20.0 ± 0.1
GNDV-6553954912	12:36:55.39	62:15:49.1	5.19	5.1 ± 0.2	27.1 ± 0.4	0.8 ± 0.4	2568 ± 1561	7^{+9}_{-5}	$8.29^{+0.52}_{-0.23}$	-19.8 ± 0.1
GNWV-7347782930	12:37:34.77	62:18:29.3	5.32	5.2 ± 0.2	26.3 ± 0.2	0.6 ± 0.3	1344 ± 666	3^{+4}_{-3}	$8.90^{+0.44}_{-0.42}$	-19.9 ± 0.1
ERSV-2213040511	03:32:21.30	−27:40:51.2	5.29	5.3 ± 0.1	25.5 ± 0.1	0.5 ± 0.2	1075 ± 394	18^{+13}_{-10}	$9.11^{+0.27}_{-0.18}$	-20.9 ± 0.1
GSWV-2454254386	03:32:45.43	−27:54:38.6	5.38	5.4 ± 0.1	24.4 ± 0.1	0.2 ± 0.1	289 ± 75	54^{+69}_{-82}	$8.96^{+0.55}_{-0.66}$	-21.6 ± 0.1
GND6418[e]	12:36:18.19	62:10:21.9	5.28	5.6 ± 0.1	23.7 ± 0.1	0.3 ± 0.1	309 ± 88	24^{+14}_{-8}	$9.99^{+0.20}_{-0.01}$	-21.6 ± 0.1
GND33928	12:37:36.87	62:18:55.9	5.35	5.2 ± 0.1	25.8 ± 0.1	0.1 ± 0.2	<222[d]	19^{+17}_{-16}	$9.09^{+0.23}_{-0.19}$	-20.4 ± 0.1
GND29175	12:37:31.45	62:17:08.3	5.25	5.3 ± 0.2	26.2 ± 0.1	0.3 ± 0.4	666 ± 929	3^{+4}_{-7}	$9.28^{+0.31}_{-0.84}$	-19.9 ± 0.1
GND12038	12:36:26.49	62:12:07.4	5.20	5.2 ± 0.4	25.8 ± 0.1	0.0 ± 0.2	254 ± 384	10^{+12}_{-9}	$9.11^{+0.43}_{-0.26}$	-20.3 ± 0.1
GS48361[e]	03:32:16.55	−27:41:03.2	5.25	5.5 ± 0.2	25.8 ± 0.1	0.3 ± 0.2	668 ± 370	6^{+6}_{-9}	$9.32^{+0.10}_{-0.53}$	-20.7 ± 0.1

Notes. [a]The spectroscopic redshifts are obtained by cross-correlating the Bouwens et al. (2015) and Skelton et al. (2014) catalogues with the spectroscopic catalogue of Stark et al. (in preparation) and Vanzella et al. (2009).
[b]Uncertainties indicate the 68 per cent confidence interval.
[c]The estimated EW for individual sources is derived by comparing the 4.5 μm flux with that derived from FAST (excluding the 4.5 μm flux from the fits).
[d]We give the error in the Hα+[N II]+[S II] EW as a 1σ upper limit when the inferred value is negative.
[e]Spectroscopic redshift measurement is based on the identification of a probable absorption line and hence less confident than the other spectroscopic redshift measurements included in this table (Stark et al. 2015, in preparation; Vanzella et al. 2009).

values in Anders & Fritze-v. Alvensleben (2003) for subsolar metallicity 0.2 $\rm Z_\odot$ and assuming case B recombination. The observed [3.6]–[4.5] colour can then be modelled by

$$[3.6]-[4.5] = ([3.6]-[4.5])_{\rm continuum} - 2.5\log_{10}\left(\frac{x_{3.6}}{x_{4.5}}\right). \quad (2)$$

Fig. 2 illustrates the contamination by nebular emission lines in the photometric filters as a function of redshift. The top panel shows the redshift ranges where the dominant emission lines, Hα, Hβ, [O III]λλ4959, 5007, [N II], and [S II] fall in the IRAC 3.6 and 4.5 μm passbands. The lower panel shows the expected [3.6]–[4.5] colour in the presence of nebular line emission. We generate two galaxy SEDs from the Binary Population and Spectral Synthesis (BPASS; Eldridge & Stanway 2012) models with a constant star formation history, but different ages and dust content and we evolve these templates through cosmic time to illustrate the predicted [3.6]–[4.5] colour. Galaxies are expected to become quite red in the redshift range $z = 5.1$–5.4, due to contamination of the 4.5 μm flux by the Hα line and no strong nebular emission line contamination in the 3.6 μm band.

The selected galaxies in the redshift range $z \sim 5.1$–5.4 allow us to deduce the EW of the nebular emission lines in $z \gtrsim 5$ objects from the fluxes in the 3.6 and 4.5 μm bands. We observe a mean [3.6]–[4.5] colour of 0.31 ± 0.05 mag for the selected sources in our photometric-redshift sample and a mean [3.6]–[4.5] colour of 0.35 ± 0.07 mag for sources in our spectroscopic sample. In both cases, we estimate the uncertainty here through bootstrap resampling.

We estimate the [3.6]–[4.5] continuum colour by contrasting the mean [3.6]–[4.5] colours observed for $z = 4.4$–5.0 spectroscopically confirmed sources from Vanzella et al. (2009), Shim et al. (2011), and Stark et al. (2013), i.e. -0.32 ± 0.03 mag, with the mean [3.6]–[4.5] colours observed for our selected $z \sim 5.1$–5.4 sample and attribute any differences in the [3.6]–[4.5] colours to the impact of flux from the Hα + [N II] + [S II] lines. Averaging over the colours of the two spectroscopic samples, we estimate a colour for the stellar continuum of [3.6]–[4.5] of 0.00 ± 0.04 mag. Here, we assume that any reddening in the continuum will in the mean affect the $z = 4.4$–5.0 sources in a similar way as our $z = 5.1$–5.4 sources, given that the two samples are close in cosmic time. While see Fig. 3 for an illustration of the differences between the two samples.

The typically red [3.6]–[4.5] colours observed for many sources in our $z = 5.1$–5.4 sample, are distinctly different from the predicted colours of low metallicity sources at $z > 5.4$ such as shown in Fig. 2. Indeed, typical $z \sim 6$ galaxy samples show blue [3.6]–[4.5] colours of ~-0.4 mag (González et al. 2012; Salmon et al. 2015). These results suggest that the IRAC [3.6]–[4.5] colour may provide significant leverage in terms of identifying galaxies that specifically lie in the narrow redshift range $z \sim 5.1$–5.4. This method has previously been explored at $z \sim 7$–8 by Smit et al. (2015a) and Roberts-Borsani et al. (2016) based on the impact of [O III] on the IRAC fluxes at these high redshifts.

3.2 Mean Hα+[N II]+[S II] EW of $z \sim 5$ Galaxies

By comparing the mean [3.6]–[4.5] colour of our $z = 5.10$–5.40 sample with the mean [3.6]–[4.5] colour of our $z = 4.4$–5.0 sample, we find an overall colour difference of 0.68±0.08 mag relative to our $z = 5.1$–5.4 photometric sample and 0.69±0.09 mag relative to our $z = 5.1$–5.4 spectroscopic sample. Comparing the colour difference, we observe with that predicted based on simple model spectra with an Hα EW of 595 Å and line ratios set by the Anders & Fritze-v. Alvensleben (2003) model (*dotted line* in Fig. 2), we infer an approximate Hα EW of 557 ± 44 Å for our $z = 5.1$–5.4 photometric sample and 592 ± 62 Å for our $z = 5.1$–5.4 spectroscopic sample.

Given that flux in the [N II] and [S II] lines would add to the colour difference observed between our $z = 4.4$–5.0 and 5.1–5.4 samples and cannot be determined separately, it is best to quote a constraint on the mean EW of Hα+[N II]+[S II]. Anders & Fritze-v. Alvensleben (2003) predict a contribution of 6.8 per cent from [N II] and 9.5 per cent from [S II]. This is in good agreement with an

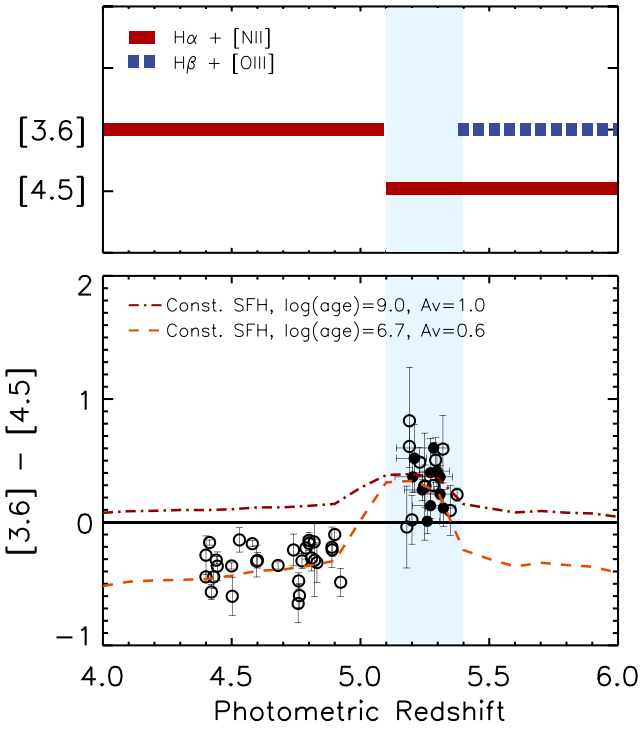

Figure 2. Nebular emission line contamination in the 3.6 and 4.5 μm photometric filters. Top panel: the redshift ranges over which the dominant nebular emission lines, Hα, Hβ, [O III], [N II], and [S II], contribute to the 3.6 and 4.5 μm flux measurements. Lower panel: the predicted [3.6]–[4.5] colour due to various nebular emission lines as a function of redshift. The solid black circles indicate sources that are selected in the redshift range $z_{\rm phot} = 5.1$–5.4, where Hα lies in the 4.5 μm filter, while 3.6 μm is devoid of strong nebular emission. Their observed [3.6]–[4.5] colours are primarily very red. The open circles are the colours for the spectroscopic sample found in Vanzella et al. (2009), which we use to estimate a stellar continuum colour of ∼ 0.00 mag. The dashed and dot–dashed lines indicate two different models from the stellar population synthesis code BPASS (Eldridge & Stanway 2012). While a galaxy with modest emission lines (rest-frame Hα+[N II]+[S II] EW∼190 Å) and significant reddening (dot–dashed line; age $=10^9$ yr, $A_V = 1.0$) can reproduce the $z \sim 5.2$ galaxy colours, the model does not reproduce the $z < 5$ galaxy colours. A young galaxy with strong emission lines (rest-frame Hα+[N II]+[S II] EW∼580 Å) and lower dust content reproduces both galaxy colour distributions at $z < 5$ and ∼5.2 (dashed line; age $=10^{6.7}$ yr, $A_V = 0.6$).

observed ratio of [N II]/Hα of 0.05–0.09 in $z \sim 2.3$ galaxies with stellar masses in the range $\log(M_*/{\rm M}_\odot) = 9.15-9.94$ by Sanders et al. (2015). If we correct for this, the mean EW in Hα+[N II]+[S II] is 665 ± 53 Å for our photometric sample and 707 ± 74 Å for our spectroscopic sample. Here, we have assumed $A_{V,\rm lines} = A_{V,\rm stars}$ such as derived by Erb et al. (2006), Reddy et al. (2010) and Shivaei et al. (2015) for $z \sim 2$ galaxies. A larger ratio of dust reddening for the nebular lines with respect to stellar light such as assumed by Calzetti et al. (2000) would result in higher derived EWs.

We can also derive Hα+[N II]+[S II] EWs for individual sources in our photometric and spectroscopic $z = 5.1$–5.4 samples. In computing the EWs for individual sources, we use FAST to fit the observed SEDs of individual sources excluding the 4.5 μm band which is contaminated by Hα emission. Then, by comparing the observed 4.5 μm flux with the expected 4.5 μm flux (without including emission lines in the FAST modelling), we derive EWs for individual sources. The results are presented in Tables 1 and 2. The mean Hα+[N II]+[S II] EW we derive for our photometric sample is

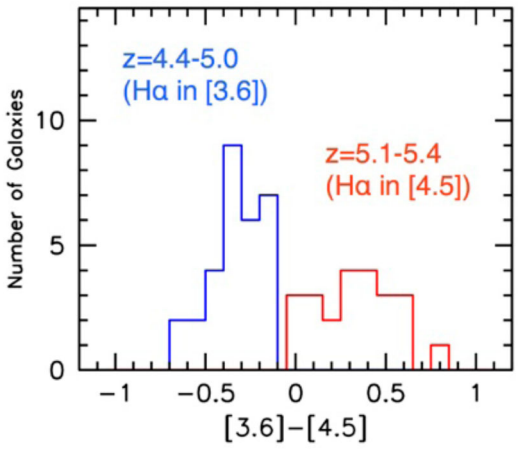

Figure 3. [3.6]–[4.5] colour distribution for sources in our $z = 5.1$–5.4 primary selection (red histogram) and $z = 4.4$–5.0 control sample (blue histogram: Appendix A). Sources where Hα+[N II] is in the [3.6] band uniformly have moderately blue colours, whereas sources with Hα+[N II] in the [4.5] band uniformly have moderately red colours. The impact of the Hα+[N II] emission lines on the IRAC [3.6]–[4.5] colour is quite clear. Deriving the Hα+[N II]+[S II] EW by contrasting the observed [3.6]–[4.5] colour of sources in the two samples should produce a very robust result.

638 ± 118 Å, while we find 855 ± 179 Å for our spectroscopic sample. If we follow the model results from Anders & Fritze-v. Alvensleben (2003) and suppose that 16.3 per cent of the 4.5 μm excess derives from [N II] and [S II], the excesses we derive suggest Hα EWs of 534 ± 99 and 715 ± 150 Å, respectively.

Fig. 4 shows several values for the Hα + [N II] + [S II] EWs with redshift from the literature. The black line gives the evolution of the Hα + [N II] + [S II] derived by Fumagalli et al. (2012) for galaxies with masses $M \sim 10^{10}$–$10^{11.5}$ ${\rm M}_\odot$, which we extrapolate to higher redshifts and lower masses (see also Sobral et al. 2014). Keeping in mind that the EW(Hα + [N II] + [S II]) as function of the redshift is higher for sources with lower stellar masses our result is consistent with the extrapolation from Fumagalli et al. (2012) and the high EWs derived by Shim et al. (2011), Stark et al. (2013) and Schenker et al. (2013).

Uncertainties in the photometric redshifts for our $z = 5.10$–5.40 sample can lead to a systematic underestimate of the Hα+[N II]+[S II] flux, if it causes us to include sources which lie outside the desired range. For $z < 5.1$ sources, the 3.6 μm band will be contaminated by Hα + [N II] + [S II] emission. Meanwhile, for $z > 5.4$ sources, Hβ + [O III] emission will contribute to the 3.6 μm band. In both cases, the [3.6]–[4.5] colour will be much bluer, causing us to infer a substantially lower EW for that source, than is truly present.

3.3 Specific star formation rates

A clean measurement of the stellar continuum emission is essential for deriving the sSFR. In our target redshift range, the flux in the 3.6 μm band can be used for this purpose, while the 4.5 μm band is contaminated by emission lines and should be left out in stellar population modelling. We derive the mean sSFR for our selected sources using similar method as described in Stark et al. (2013). We derive stellar masses using the modelling code FAST (Kriek et al. 2009), which fits stellar population synthesis templates from Bruzual & Charlot (2003) to broad-band photometry. For consistency, we assume a Salpeter (1955) IMF with 0.1–100 ${\rm M}_\odot$, a

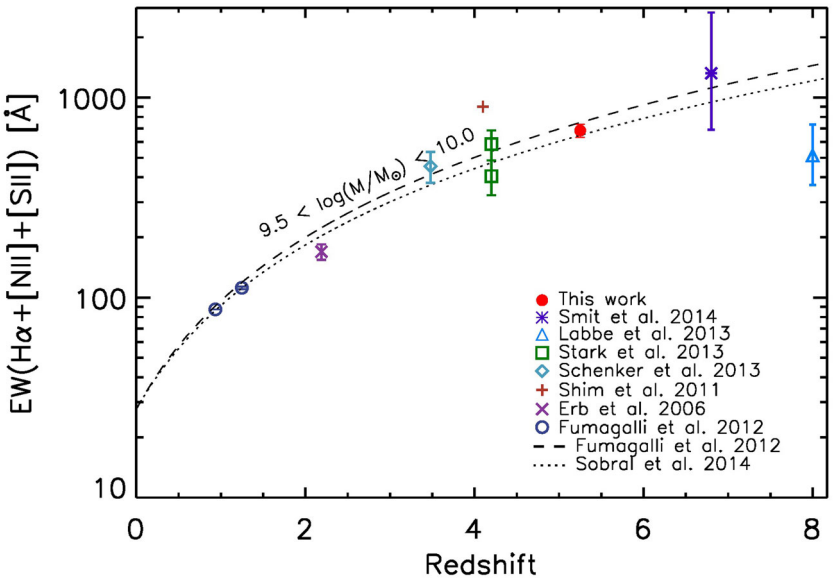

Figure 4. Hα+[N II]+[S II] EWs as function of redshift derived from the mean [3.6]–[4.5] colour of our source selection. Several estimates from the literature are indicated for reference (Erb et al. 2006; Shim et al. 2011; Fumagalli et al. 2012; Schenker et al. 2013; Stark et al. 2013). The upper and lower EW determination for Stark et al. (2013) excludes and does not exclude the contaminated IRAC band in deriving the stellar continuum required to derive the EW for the Hα+[N II]+[S II] line. We assume line ratios as listed by Anders & Fritze-v. Alvensleben (2003) and that the stellar continuum of our $z = 5.10$–5.40 sample has a [3.6]–[4.5] colour of 0.00 $\pm$0.04 mag. Redder [3.6]–[4.5] colours will therefore be due to the emission lines contaminating the 4.5 μm flux. The measured Hα+[N II]+[S II] EW shown here represents the weighted mean of our EW estimates from our photometric and spectroscopic $z = 5.1$–5.4 samples (i.e. 684$\pm$51 Å) and is higher than values derived at lower redshifts, suggesting stronger line emission at $z \sim 5$. The evolution of Hα+[N II]+[S II] EW for the indicated stellar mass range found by Fumagalli et al. (2012) is extrapolated (given by the dashed line) and is consistent with our inferred Hα+[N II]+[S II] EW.

subsolar metallicity $Z = 0.2$ Z$_\odot$ and dust attenuation from Calzetti et al. (2000). The ages range from 10 Myr to the age of the Universe at the redshift of the source. The star formation history is assumed to be constant and the dust content is varied between $A_V = 0$ and 3 mag. Given the sensitivity of our inferred SFRs to the fundamental degeneracy between dust and age in fitting to the observed photometry (i.e. where either dust or age can be effective in fitting to the redder UV slopes or ∼3600 Å breaks), we derive SFRs directly from the UV continuum, using the Kennicutt (1998) relation and fixing the dust extinction using the relationship from Meurer et al. (1999) between A_V and the UV-continuum slope β. We remark that in adopting this approach, our procedure we utilize slightly different assumptions for deriving SFRs and stellar masses and therefore our approach includes a slight internal tension. Fortunately, stellar mass is a parameter that is fairly robust against the degeneracy between age and dust mentioned above and therefore we can reliably use these stellar mass measurements. From this method, we derive a median sSFR of 17^{+2}_{-5} Gyr^{-1} (individual sSFR estimates are listed in Tables 1 and 2).

We also explore the use of an Small Magellanic Cloud dust-law, which might seem more appropriate for Lyman-break galaxies at $z \sim 5$–6 based on recent ALMA results by Capak et al. (2015). We fit FAST models as above with a Noll et al. (2009) dust law with parameters $E_b = 0.01$ and $\delta = -0.42$ and find an sSFR of ∼13 Gyr^{-1}.

It is useful to compare the median sSFR estimates we find here, 17^{+2}_{-5} and 13 Gyr^{-1}, with previous estimates. This represents a $7^{+1}_{-2}\times$ increase in sSFR compared to the 2.4 Gyr^{-1} value found at $z \sim 2$ (Reddy et al. 2012a), supporting a significant evolution in the sSFR. The typical stellar mass for galaxies in our $z = 5.1$–5.4 selection is ∼10^9 M$_\odot$, so we will make our comparison with previous measures at this stellar mass. Both Stark et al. (2013) and González et al. (2014) find that the typical galaxy with this stellar mass has a UV luminosity M_{UV} of −20 mag. Accounting for a factor of ∼2 mean dust attenuation at this luminosity (as implied by the Bouwens et al. 2014 $\beta \sim -1.9$ results), the equivalent sSFR is ∼11 Gyr^{-1}. Somewhat similarly, Salmon et al. (2015) derive an sSFR of $\sim 8^{+8}_{-4}$ Gyr^{-1}, which is again somewhat lower than we find here.

All things being equal, we would expect the sSFR estimates we derive here to be more accurate than previous estimates, given our precise knowledge of the redshifts and hence the position of nebular emission lines within galaxies. The impact of the lines on the mass and sSFR estimates could be as large as a factor of ∼1.5, allowing for an approximate reconciliation of the present sSFR estimates with that from previous work. However, the present sample of $z \sim 5.1$–5.4 galaxies is still quite small, and therefore expansion of the present sample would certainly be helpful for improving our sSFR estimate.

3.4 Possible dependence of the EW of Hα+[N II]+[S II] on the stellar mass

By fitting to the photometry of all passbands uncontaminated by the strong Hα+[N II]+[S II] nebular emission lines, we can estimate stellar masses for sources in our $z = 5.1$–5.4 samples, as described in the previous section. As these sources are distributed over a wide range of stellar mass, i.e. $10^{8.5}$–$10^{10.4}$ M$_\odot$, we can go beyond a simple determination of the mean Hα+[N II]+[S II] EW for $z \sim 5$ galaxies and look at whether there is a dependence on stellar mass.

Any significant dependence on stellar mass would be noteworthy, as it could point to a significant mass or scale dependence to the star formation histories of galaxies. While such a scale dependence could be expected if there are significant feedback effects at early times (e.g. Bowler et al. 2014; Bouwens et al. 2015), many

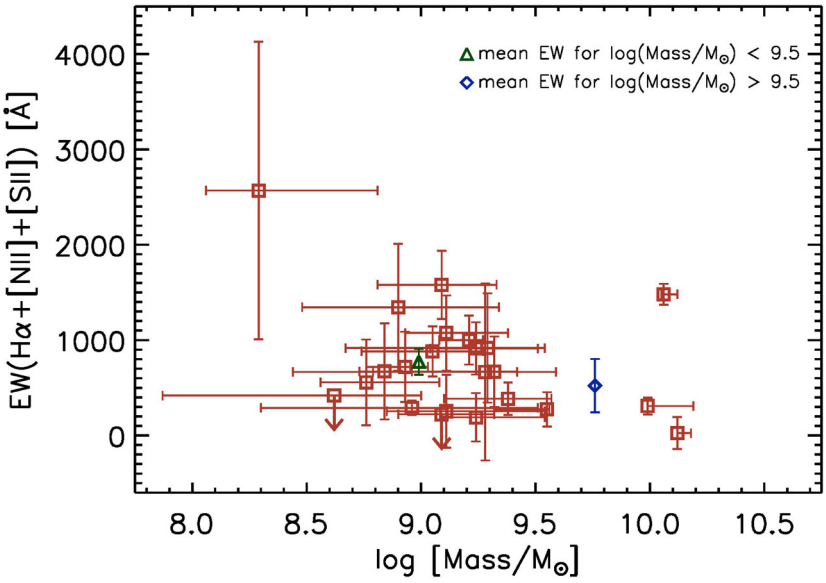

Figure 5. The estimated Hα+[N II]+[S II] EW from the 4.5 μm excess versus the estimated stellar mass (red squares with 1σ error bars). The mean Hα+[N II]+[S II] EW we estimate for sources with an estimated stellar mass $> 10^{9.5}$ $M_\odot$ is 522 ± 279 Å (blue diamond), while the mean Hα+[N II]+[S II] EW we estimate for sources with an estimated stellar mass $< 10^{9.5}$ $M_\odot$ is 773 ± 136 Å (green triangle). The present results provide no strong evidence for a correlation between the inferred Hα+[N II]+[S II] EWs and the stellar mass. However, we emphasize that this may change as the samples and dynamical masses become larger.

simulations (e.g. Finlator, Oppenheimer & Davé 2011) predict that galaxies build up their stellar mass in a relatively self-similar manner, independent on the overall stellar mass.

We examine the evidence for such a correlation between the Hα+[N II]+[S II] EW and the stellar mass in Fig. 5, plotting the Hα+[N II]+[S II] EWs we estimate for individual sources against the stellar masses we estimate for the same sources. Also shown on this figure is the average Hα EW, we measure for galaxies with estimated stellar masses $<10^{9.5}$ $M_\odot$ (773 ± 136 Å) and for those with estimated stellar masses $>10^{9.5}$ $M_\odot$ (522 ± 279 Å).

At face value, these results do not provide any strong evidence ($<2\sigma$) for a correlation between the Hα EW and the stellar mass. While it is possible that a slight correlation might be expected (i.e. since massive galaxies would be the first to experience a slowing in their growth rate due to feedback-type effects), no strong trend is evident. A similar conclusion can be drawn by fitting Hα+[N II]+[S II] EWs versus stellar mass relation to a straight line. Our results in Fig. 5 are in broad agreement with literature studies using SED fitting techniques (e.g. Schaerer, de Barros & Sklias 2013).

4 DISCUSSION AND SUMMARY

In this paper, we derive the Hα+[N II]+[S II] EW and the sSFR by selecting galaxies at $z \sim 5.1$–5.4. In doing so, we make use of the highest redshift window allowing for a clean measurement of both the Hα flux and the stellar continuum. Reliable estimates of the stellar mass and sSFR require a clean measurement of the stellar continuum. At $z = 5.4$–6.6, rest-frame optical flux information on galaxies – as derived from the *Spitzer*/IRAC data – can be quite ambiguous to interpret, due to a significant contribution from nebular emission lines (Hα, Hβ, [O III], [N II], [S II]) in both sensitive *Spitzer*/IRAC channels (i.e. [3.6] and [4.5]), and at $z > 6.6$, the Hα line redshifts out of the [4.5] channel.

Observing galaxies in the $z = 5.1$–5.4 redshift interval is useful as a contrast and for interpreting the observations of galaxies in the redshift interval $z = 3.8$–5.0. In both intervals, the *Spitzer*/IRAC fluxes are expected to be dominated by a stellar continuum contribution and a contribution from Hα. However, the Hα line will contribute to the measured flux in a different *Spitzer*/IRAC band at $z = 5.1$–5.4 ([4.5]) than at $z = 3.8$–5.0 ([3.6]), so the colours of galaxies in the two samples can be contrasted and used to set strong constraints on the rest-frame EW of Hα.

In our utilization of the $z = 5.1$–5.4 redshift interval to study the Hα EW and sSFR, we have selected 11 bright sources over the CANDLES GOODS-North and GOODS-South fields satisfying the criteria S(H_{160})/N(3.6 μm) > 3, S(H_{160})/N(4.5 μm) > 3, ($V_{606} - i_{775} > 1.2$), ($z_{850} - H_{160} < 1.3$), ($V_{606} - i_{775} > 0.8$ ($z_{850} - H_{160}$) + 1.2), and S/N(B_{435}) < 2. The candidates are required to have > 85 per cent probability of lying in the redshift range $z \sim 5.1$–5.4. We have supplemented this sample with 13 $z = 5.10$–5.40 sources from the spectroscopic redshift sample of Vanzella et al. (2009) and Stark et al. (in preparation).

We find a mean rest-frame EW(Hα+[N II]+[S II]) of 665 ± 53 Å for our photometric sample and 707 ± 74 Å for our spectroscopic sample based on the mean [3.6]–[4.5] colours of these samples. Assuming that 84 per cent of the Hα+[N II]+[S II] line flux is Hα, we further derive an Hα EW of ∼ 557±44 and 592 ±62 Å for our photometric and spectroscopic sample, respectively. Our estimate is consistent with the $(1+z)^{1.8}$ power law derived for a strong line-emitter model by Fumagalli et al. (2012).

Our selection at $z \sim 5$ has a median sSFR of $\sim 17^{+2}_{-5}$ Gyr^{-1}. This represents a 7^{+1}_{-2} × increase in sSFR compared to the 2.4 Gyr^{-1} value found at $z \sim 2$ (Reddy et al. 2012a), supporting a significant evolution in the sSFR. Our estimate is in agreement with the theoretical model of Neistein & Dekel (2008), matching the increasing specific inflow rate of baryonic particles.

We emphasize the Hα+[N II]+[S II] EWs and sSFR we derive here for our photometric sample is effectively a lower limit on the true value, as the inclusion of any sources in our photometric selection outside the desired redshift range due to photometric redshift

uncertainties would result in a bluer mean [3.6]–[4.5] colour and higher redshift optical flux for the average source.

We also take advantage of the stellar population modelling we do of individual sources in our sample and the range of estimated masses to look at a possible correlation between the Hα+[N II]+[S II] EW of sources in our selection and their stellar masses. We find no strong evidence ($<2\sigma$) for there being a correlation between the EW of Hα+[N II]+[S II] EWs and the stellar mass. However, we caution that our sample sizes and dynamic range are limited, and so a correlation may be evident when examining large sample sizes or a wider dynamic range.

More accurate results would require spectroscopic redshifts for a larger number of sources. Though our target redshift range allows for a relatively clean measurement, constructing large samples of $z \sim 5.1$–5.4 galaxies is challenging due to the narrow redshift window we are considering. We expect significant progress in the future as a result of future samples with the MUSE spectrograph (Bacon et al. 2015). Furthermore, ultradeep *Spitzer*/IRAC data over the GOODS-North and GOODS-South fields will become available through the GOODS Re-ionization Era wide-Area Treasury from *Spitzer* (GREATS, PI: Labbé) programme (2014).

ACKNOWLEDGEMENTS

We acknowledge the support of NASA grant NAG5-7697, NASA/STScI grant *HST*-GO-11563, and an NWO vrij-competitie grant 600.065.140.11N211. RS acknowledges the support of the Leverhulme Trust. This research has made use of the NASA/IPAC Infrared Science Archive, which is operated by the Jet Propulsion Laboratory, California Institute of Technology, under contract with the National Aeronautics and Space Administration.

REFERENCES

Anders P., Fritze-v. Alvensleben U., 2003, A&A, 401, 1063
Ashby M. L. N. et al., 2013, ApJ, 769, 80
Ashby M. L. N. et al., 2015, ApJS, 218, 33
Bacon R. et al., 2015, A&A, 575, A75
Bouché N., Dekel A., Genzel R., Cresci G., Förster Schreiber N. M., Shapiro K. L., Davies R. I., Tacconi L., 2010, ApJ, 718, 1001
Bouwens R. J. et al., 2009, ApJ, 705, 936
Bouwens R. J. et al., 2012, ApJ, 754, 83
Bouwens R. J. et al., 2014, ApJ, 793, 115
Bouwens R. J. et al., 2015, ApJ, 803, 34
Bowler R. A. A. et al., 2014, MNRAS, 440, 2810
Brammer G. B., van Dokkum P. G., Coppi P., 2008, ApJ, 686, 1503
Bruzual G., Charlot S., 2003, MNRAS, 344, 1000
Calzetti D., Armus L., Bohlin R. C., Kinney A. L., Koornneef J., Storchi-Bergmann T., 2000, ApJ, 533, 682
Capak P. L. et al., 2015, Nature, 522, 455
Castellano M. et al., 2014, A&A, 566, A19
de Barros S., Schaerer D., Stark D. P., 2014, A&A, 563, A81
Eldridge J. J., Stanway E. R., 2012, MNRAS, 419, 479
Erb D. K., Steidel C. C., Shapley A. E., Pettini M., Steidel C. C., Reddy N. A., Adelberger K. L., 2006, ApJ, 647, 128
Eyles L. P., Bunker A. J., Stanway E. R., Lacy M., Ellis R. S., Doherty M., 2005, MNRAS, 364, 443
Finkelstein S. L. et al., 2012, ApJ, 756, 164
Finlator K., Davé R., Oppenheimer B. D., 2007, MNRAS, 376, 1861
Finlator K., Oppenheimer B. D., Davé R., 2011, MNRAS, 410, 1703
Fumagalli M. et al., 2012, ApJS, 757, L22
Giavalisco M. et al., 2004, ApJ, 600, L93
González V., Labbé I., Bouwens R. J., Illingworth G. D., Franx M., Kriek M., Brammer G. B., 2010, ApJ, 713, 115
González V., Bouwens R. J., Labbé I., Illingworth G., Oesch P., Franx M., Magee D., 2012, ApJ, 755, 148
González V., Bouwens R. J., Illingworth G., Labbeé I., Oesch P., Franx M., Magee D., 2014, ApJ, 781, 34
Grogin N. A. et al., 2011, ApJS, 197, 35
Holden B. P. et al., 2016, ApJ, 820, 73
Kennicutt R. C., Jr, 1998, A&A, 36, 189
Koekemoer A. M. et al., 2011, ApJS, 197, 36
Kriek M., van Dokkum P. G., Labbé I., Franx M., Illingworth G. D., Marchesini D., Quadri R. F., 2009, ApJ, 700, 221
Kron R. G., 1980, ApJS, 43, 305
Labbé I. et al., 2010a, ApJ, 708, L26
Labbé I. et al., 2010b, ApJ, 716, L103
Labbé I. et al., 2013, ApJ, 777, L19
Labbé I. et al., 2014, Spitzer Proposal, 11134
Labbé I. et al., 2015, ApJS, 221, 23
Meurer G. R., Heckman T. M., Calzetti D., 1999, ApJ, 521, 64
Neistein E., Dekel A., 2008, MNRAS, 388, 1792
Noll S., Burgarella D., Giovannoli E., Buat V., Marcillac D., Muñoz-Mateos J. C., 2009, A&A, 507, 1793
Oesch P. A. et al., 2013, ApJ, 772, 136
Oke J. B., Gunn J. E., 1983, ApJ, 266, 713
Reddy N. A., Erb D. K., Pettini M., Steidel C. C., Shapley A. E., 2010, ApJ, 712, 1070
Reddy N. et al., 2012a, ApJ, 744, 154
Reddy N. A., Pettini M., Steidel C. C., Shapley A. E., Erb D. K., Law D. R., 2012b, ApJ, 754, 25
Roberts-Borsani G. W. et al., 2016, ApJ, 823, 143
Salmon B. et al., 2015, ApJ, 799, 183
Salpeter E. E., 1955, ApJ, 121, 161
Sanders R. L. et al., 2015, ApJ, 799, 138
Schaerer D., de Barros S., 2009, A&A, 502, 423
Schaerer D., de Barros S., 2010, A&A, 515, A73
Schaerer D., de Barros S., Sklias P., 2013, A&A, 549, A4
Schenker M. A., Ellis R. S., Konidaris N. P., Stark D. P., 2013, ApJ, 777, 67
Shim H., Chary R.-R., Dickinson M., Lin L., Spinrad H., Stern D., Yan C.-H., 2011, ApJ, 738, 69
Shivaei I., Reddy N. A., Steidel C. C., Shapley A. E., 2015, ApJ, 804, 149
Skelton R. E. et al., 2014, ApJS, 214, 24
Smit R. et al., 2014, ApJ, 784, 58
Smit R. et al., 2015a, ApJ, 801, 122
Smit R., Bouwens R. J., Labbé I., Franx M., Wilkins S. M., Oesch P. A., 2015b, ApJ, preprint (arXiv:1511.08808)
Sobral D., Best P. N., Smail I., Mobasher B., Stott J., Nisbet D., 2014, MNRAS, 437, 3516
Stark D. P., Ellis R. S., Bunker A., Bundy K., Targett T., Benson A., Lacy M., 2009, ApJ, 697, 1493
Stark D. P., Ellis R. S., Chiu K., Ouchi M., Bunker A., 2010, MNRAS, 408, 1628
Stark D. P., Schenker M. A., Ellis R., Robertson B., McLure R., Dunlop J., 2013, ApJ, 763, 129
Vanzella E. et al., 2009, ApJ, 695, 1163
Weinmann S. M., Neistein E., Dekel A., 2011, MNRAS, 417, 2737
Windhorst R. A. et al., 2011, ApJS, 193, 27
Yabe K., Ohta K., Iwata I., Sawicki M., Tamura N., Akiyama M., Aoki K., 2009, ApJ, 693, 507
Yan H., Dickinson M., Giavalisco M., Stern D., Eisenhardt P. R. M., Ferguson H. C., 2006, ApJ, 651, 24

APPENDIX A: $z = 4.4$–5.0 REFERENCE SAMPLE

In order to estimate the mean stellar continuum colour [3.6]–[4.5] for $z \sim 5$ (Section 3.1), we make use of a spectroscopic selection of sources at $z = 4.4$–5.0 from Vanzella et al. (2009), Shim et al. (2011), and Stark et al. (2013). We obtain a sample of 30 $z = 4.4$–5.0 sources by cross-correlating the source catalogues of Bouwens

Table A1. Our reference sample of spectroscopically confirmed sources in the redshift range $z \sim 4.4$–5.0. The sources are obtained by matching the spectroscopic redshift sample listed in Vanzella et al. (2009) with the Bouwens et al. (2015) catalogue. Source IDs are as in the Bouwens et al. (2015), Shim et al. (2011), or Stark et al. (2013) catalogues.

ID	RA	Dec.	z_{spec}	[3.6]	[3.6]–[4.5]
GSWV-2426242897	03:32:42.62	−27:54:28.97	4.400	24.0 ± 0.1	−0.5 ± 0.1
GSDV-2228872758	03:32:22.88	−27:47:27.58	4.440	23.8 ± 0.1	−0.3 ± 0.1
GSDV-2229762901	03:32:22.97	−27:46:29.01	4.500	23.3 ± 0.1	−0.4 ± 0.1
ERSV-2285605575	03:32:28.56	−27:40:55.75	4.597	24.6 ± 0.1	−0.2 ± 0.2
GSDV-2169812296	03:32:16.98	−27:51:22.96	4.600	24.0 ± 0.1	−0.4 ± 0.1
GSWV-2475822816	03:32:47.58	−27:52:28.16	4.758	25.2 ± 0.1	−0.7 ± 0.2
GSDV-2435391920	03:32:43.53	−27:49:19.20	4.763	25.0 ± 0.1	−0.6 ± 0.1
GSDV-2401153550	03:32:40.11	−27:45:35.50	4.773	24.6 ± 0.1	−0.3 ± 0.1
GSDV-2219353310	03:32:21.93	−27:45:33.10	4.788	24.6 ± 0.1	−0.2 ± 0.1
ERSV-2052630041	03:32:05.26	−27:43:00.41	4.801	24.5 ± 0.1	−0.2 ± 0.1
GSDV-2426693897	03:32:42.66	−27:49:38.97	4.831	25.6 ± 0.1	−0.2 ± 0.2
S33166	03:32:58.38	−27:53:39.58	4.40	24.8 ± 0.1	−0.3 ± 0.2
N12138	12:36:42.25	62:15:23.25	4.414	23.3 ± 0.1	−0.2 ± 0.1
N23791	12:37:20.58	62:11:06.11	4.421	23.7 ± 0.1	−0.6 ± 0.1
S31908	03:32:54.04	−27:50:00.81	4.43	24.7 ± 0.1	−0.4 ± 0.1
N13279	12:36:46.16	62:07:01.83	4.444	24.1 ± 0.1	−0.4 ± 0.1
N24628	12:37:23.57	62:20:38.72	4.502	24.4 ± 0.1	−0.6 ± 0.2
N28987	12:37:19.69	62:15:42.46	4.53	24.6 ± 0.1	−0.1 ± 0.1
N12849	12:36:44.68	62:11:50.62	4.580	23.2 ± 0.1	−0.2 ± 0.1
N31130	12:37:57.51	62:17:19.10	4.680	23.2 ± 0.1	−0.4 ± 0.1
S6294	03:32:14.50	−27:49:32.69	4.74	24.8 ± 0.1	−0.2 ± 0.1
S32900	03:32:57.17	−27:51:45.01	4.76	24.1 ± 0.1	−0.5 ± 0.1
S1745	03:32:05.26	−27:43:00.42	4.80	24.6 ± 0.1	−0.1 ± 0.1
S3792	03:32:10.03	−27:41:32.65	4.81	24.1 ± 0.1	−0.3 ± 0.1
S1669	03:32:05.08	−27:46:56.52	4.82	22.7 ± 0.1	−0.2 ± 0.1
N23039	12:37:18.07	62:16:41.72	4.822	26.1 ± 0.1	−0.3 ± 0.3
N6738	12:36:23.56	62:15:20.30	4.889	25.2 ± 0.1	−0.2 ± 0.2
N6333	12:36:21.94	62:15:17.12	4.890	23.9 ± 0.1	−0.2 ± 0.1
S20041	03:32:33.48	−27:50:30.00	4.90	23.9 ± 0.1	−0.1 ± 0.1
S23745	03:32:44.07	−27:42:27.43	4.923	24.3 ± 0.1	−0.5 ± 0.1

et al. (2015) and Skelton et al. (2014) with the spectroscopic catalogue of Shim et al. (2011), Stark et al. (2013) and Vanzella et al. (2009). As in Section 2.3, we exclude any sources which are reported to have detected X-ray counterparts or AGN emission lines by Shim et al. (2011), Vanzella et al. (2009) and Stark et al. (2013). The excluded sources including those with the following coordinates (03:32:29.29, −27:56:19.5; 03:32:44.11, −27:54:52.5; 12:36:42.05, 62:13:31.7; 03:32:33.77, −27:52:23.7). We tabulate the measured [3.6]–[4.5] colours and coordinates of the sources we utilize in Table A1.

This paper has been typeset from a TEX/LATEX file prepared by the author.